

“This is a post-peer-review, pre-copyedit version of an article published in

Nguyen, N., Johannessen, A., Rooth, S. & Hanke, U. (2018). The impact of area on BAW resonator performance and an approach to device miniaturization. *Ultrasonics*.

The final authenticated version is available online at:

doi: <https://doi.org/10.1016/j.ultras.2018.11.014>

The Impact of Area on BAW Resonator Performance and an Approach to Device Miniaturization

Ngoc Nguyen^a, Agne Johannessen^a, Stig Rooth^b, Ulrik Hanke^{a,*}

^a*Department of Microsystems, University of South-Eastern Norway, Raveien 215, 3184
Borre, Norway*

^b*Kongsberg Norspace AS, Knudsrødveien 7, 3189 Horten, Norway*

Abstract

The dependence of the performance of thin film bulk acoustic resonator (FBAR) and solidly mounted resonator (SMR), on their areas is studied with the aid of finite element method (FEM) software. Dual step frame method is applied for both types of the resonators in order to improve their quality factors at resonance and at antiresonance frequency when they are miniaturized. The important role of the material quality in promoting the benefit of this method is also emphasized in this study.

Keywords: FBAR, SMR, BAW resonator filters

1. Introduction

2 The fast growth of mobile handsets worldwide in the past decade has cre-
3 ated demanding needs for analog filter modules in terms of high performance
4 and their number per mobile device. The manufacturers keep adding new
5 frequency bands to their next generation smartphones whenever the authori-
6 ties release the bands. Consequently, the number of analog filter modules per
7 mobile device has recently escalated to 60 and will increase to 100+ due to
8 the evolution of mobile phone technology into 5G [1], [2]. This leads to two
9 challenges: overcrowding of physical space and coexistence of many frequency
10 bands a device supports. Filter modules based on bulk acoustic wave (BAW)
11 resonators fulfill the requirements of low cost, high performance, small size

*Corresponding Author: Ulrik Hanke, Raveien 215, 3184 Borre, Norway; Email: ulrik.hanke@usn.no; Phone: +47 310 09 023

12 and yet good power handling capability [3]. However, placing so many ana-
13 log filters and multiplexers into a cellphone with limited space for the RF
14 front-end module implies either using tunable filters or enhanced miniatur-
15 ization of the filter devices, along with a smart packaging strategy. Tunable
16 BAW filters, for which some physical restrictions have to be overcome, were
17 reported to provide limited tuning range of frequency and low quality factors
18 (Q) [4], [5]. In addition, the filters must provide high selectivity, i.e. their
19 BAW resonator core elements must have high Q factors, in order to resolve
20 the coexistence challenge in demanding applications. However, this may lead
21 to a sacrifice in the filter bandwidth.

22 The performance parameters of a BAW resonator are substantially influ-
23 enced by its area. At resonance frequency f_r of the BAW resonators, due to
24 the high current, ohmic loss dominates, leading to the deterioration of the
25 quality factor Q_r while at antiresonance frequency f_a the acoustic leakage
26 is one of the main loss mechanisms that worsen Q_a [6], [7]. As the area of
27 the resonator increases, the electrical current increases hence the effect of
28 ohmic loss is more pronounced. This contributes to the increase of Q_r for
29 smaller resonator areas down to a size where Q_r drops. On the other hand, it
30 is reported that reducing the resonator size leads to the decrease in coupling
31 coefficient and Q_a [8]. Miniaturization of the resonator in order to integrate
32 more analog filters into the RF front-end module, and thus more channels
33 into a given frequency range is meaningless if Q_a degrades too much, i.e.
34 results in too poor steepness of the filter skirt [9]. A method to improve the
35 Q_a for small size resonators is therefore essential. A possible strategy is to
36 reduce the acoustic leakage at f_a using a dual step frame design [10], [11] for
37 dual Lamb mode reflection or double-raised borders [12]. In this paper, the
38 dual step frame design is carried out for both types of BAW resonators – thin
39 film bulk acoustic resonator (FBAR) and solidly mounted resonator (SMR).
40 For the SMR, the design procedure also takes into account the reflection of
41 vertically propagating shear waves, apart from the fundamental longitudinal
42 waves, in order to minimize the acoustic loss through the vertical acoustic
43 mirror [13].

44 FEM simulations are used to study the behavior and evaluate the per-
45 formance of the BAW designs, including those with no frame, with a single
46 step frame, and with a dual step frame. The active area is varied from
47 $625\ \mu\text{m}^2$ up to $90000\ \mu\text{m}^2$ for the FBAR case. For the SMR case, based on
48 the conclusions from the FBAR results, the area is varied from $3600\ \mu\text{m}^2$ up
49 to $90000\ \mu\text{m}^2$. In order to investigate how material losses influence the use-

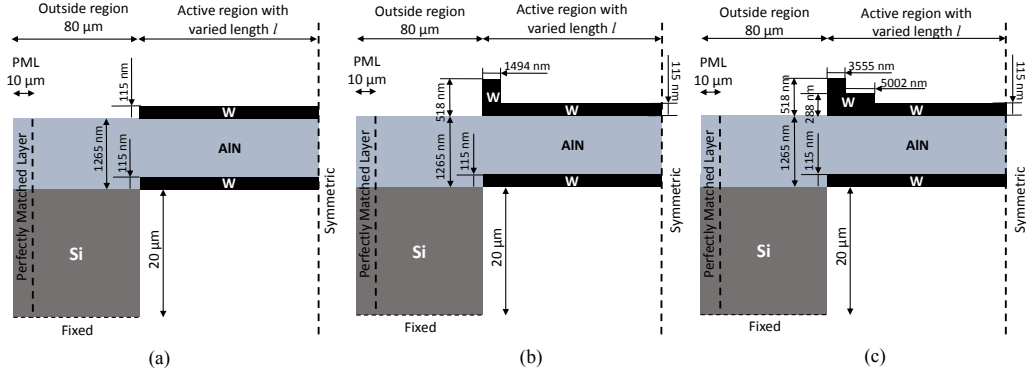


Figure 1: 2D schematics of the simulated FBARs without frame (a), with a single frame (b), and with a dual step frame (c). The value of l ranges from 12.5 to 150 μm . The resonators are not drawn to scale.

50 fulness of the dual step frame strategy, simulations with varying material loss
 51 parameters are performed. The results show that miniaturization of BAW
 52 resonators without degrading Q factors is achievable, given that a proper
 53 dual step frame design is applied. Further, the impact of the optimized dual
 54 step frame design is higher for lower material acoustic loss factors.

55 2. FBAR

56 2.1. Analysis of thickness-extensional (TE_1) resonance for a 1D FBAR with 57 finite electrode area

58 Standard models used to estimate FBAR performance, like the 1D Ma-
 59 son model, neglects the influence of the mechanical and electrical boundary
 60 conditions along the electrode perimeter for finite electrode dimensions. It
 61 is shown in [14] that for thin piezoelectric plates the boundary conditions
 62 reduce to the continuity of vertical displacements and their derivatives. By
 63 this simplification an approximate analytical expression for the admittance Y
 64 of the TE_1 trapped energy resonance of the 2D FBAR design with electrode
 65 length $2l$ shown in Fig A.1(b) in the appendix can be found by applying the
 66 method proposed in [15].

$$Y(f, l) = \frac{I(f, l)}{V} = \frac{4j\omega l^2 \varepsilon_{33}^f}{h^f} (\widehat{k}^2 + 1) + \frac{8j\omega l \varepsilon_{33}^f \widehat{k}^2 (G_1^n)^2 (\eta_{fn}^0)^2 \sin^2(\bar{\xi}_{n\mu} l)}{\left(\frac{\widehat{\omega}_{n\mu}^2}{\omega^2} - 1\right) G_2^n (h^f)^2 (\bar{\xi}_{n\mu})^2 L_{n\mu}} \quad (1)$$

67 Here the current flowing into the FBAR is I and the voltage applied is V .
68 $\omega = 2\pi f$ is the angular frequency and $\widehat{\omega}_{n\mu} = 2\pi f_r$ is the angular frequency
69 of the trapped TE_1 mode. Details of derivation and parameter definitions
70 are given in the appendix of this paper. Both resonance frequency f_r of
71 this trapped TE_1 mode, happening when Y is maximum, and antiresonance
72 frequency f_a , occurring when Y is minimum, depend on the electrode area
73 $2l \times 2l$ of the FBAR.

74 2.2. Modeling and Simulation Setup

75 The active region of an FBAR comprises of a piezoelectric layer sand-
76 wiched between two metal electrodes. This stratified structure with free top
77 and bottom surfaces makes the FBAR a robust acoustic resonator in terms
78 of energy confinement for the bulk waves traveling in the vertical direction.
79 However, at the periphery of the active region, the resonator suffers from
80 energy loss due to the lateral leakage of propagating Lamb waves. This type
81 of loss has significant contribution at f_a [7], leading to the degradation of
82 the Q_a . In order to diminish the loss, a frame with two steps is added to the
83 perimeter region of the resonator. The performance of this dual-step framed
84 resonator design is compared to those of other FBAR designs as their active
85 areas are varied.

86 Fig. 1 shows the geometries and the used materials of the 2D FEM mod-
87 els built in COMSOL for three design cases. The first one (Fig.1(a)) is a
88 conventional FBAR with no frame. The second one (Fig.1(b)) is an FBAR
89 with a single step frame whose width is three quarter wavelengths of the
90 S_1 mode which is in line with literature [6], [16]. This structure provides a
91 high impedance at f_a and thus high Q_a . The third design case, as shown in
92 Fig. 1(c), is an FBAR with a dual step frame designed to be a lateral acoustic
93 mirror that can reflect the two propagating Lamb modes S_1 and A_1 . The
94 width of each step is approximately equal to an odd multiple of the quarter
95 wavelength for both S_1 and A_1 modes. The detailed procedure for the de-
96 sign of this frame structure is described in [10]. As indicated in the figure,
97 symmetry is utilized so only half of the resonator geometry is included in the

Parameters	AlN	W	Si	SiO ₂	Ir
Density (kg/m ³)	3260	19350	2181	2200	22350
Longitudinal wave velocity (m/s)	11350	5210	8860	6200	5350
Shear wave velocity (m/s)	6090	2880	5310	3950	3240
Resistivity (Ωm)	–	5.6e-8	–	–	4.7e-8
Mechanical loss factor η_s	2.5e-4	5e-4	6e-5	8.4e-4	1.7e-3
Dielectric loss factor	2.0e-3	–	–	–	–

Table 1: Material parameters [18, 19, 20, 21]

98 FEM model in order to reduce the simulation time and memory use. All the
99 three resonators have the same area of the active region, i.e. the overlapping
100 area between the top and bottom electrodes. The thicknesses of the layers
101 in the “non-framed” part of the FBAR active regions are chosen so that the
102 resonance frequency is at 2.42 GHz and the antiresonance frequency is at
103 2.49 GHz for $100 \times 100 \mu\text{m}^2$ area. AlN is chosen as the piezoelectric material
104 because it offers low acoustic loss, high acoustic velocity and the capability
105 for CMOS integration. In order to achieve good electromechanical coupling
106 coefficients for the resonators the thickness ratio of the AlN layer and the
107 electrodes is optimized. The outside regions are terminated with perfectly
108 matched layers (PMLs) in order to avoid the artificially reflected waves from
109 the edges of the structure. Although all the FEM simulation models are 2D,
110 the widths of the active regions are selected to be the same as the lengths $2l$
111 since this value is required for the calculation of the static capacitance and
112 electrical response. This means that the active regions of all the simulated
113 FBAR designs are squares. The mesh size in the active region for all the
114 models is chosen to be 100 nm, which is smaller than one tenth of the small-
115 est wavelength among the propagating Lamb modes at f_a . The parameters of
116 the materials used in the designs are listed in Table 1. In the simulations, all
117 the materials except AlN are assumed to be isotropic. In the case of AlN – a
118 piezoelectric material that has wurtzite crystalline structure with hexagonal
119 symmetry – the stiffness constants, permittivity and coupling coefficients
120 are obtained from [17].

121 The ohmic loss due to finite electrode conductivity is included in the
122 simulations by connecting an external series resistor R_s to the resonator
123 via the electrical circuit module in COMSOL. At resonance frequency, this
124 resistor represents the damping of the resonator to which it is connected. The
125 value of R_s approximately equals the DC resistance of the electrodes, i.e. the

126 loss due to eddy currents caused by spurious modes is neglected. Therefore,
 127 this value may deviate from the correct value for frequencies below and close
 128 to f_r where a relatively large number of strong spurious modes are located.
 129 The length l is varied from 12.5 μm to 150 μm in order to examine the effect
 130 of area on the overall performance for all the resonator designs depicted in
 131 Fig. 1. The Q factors and effective electromechanical coupling factor k_{eff}^2 are
 132 calculated from

$$Q_{r,a} = \pm \frac{f_{r,a}}{2} \left. \frac{d\angle Z}{df} \right|_{f=f_{r,a}} \quad (2)$$

133

$$k_{eff}^2 = \frac{\pi f_r}{2 f_a} \frac{1}{\tan\left(\frac{\pi f_r}{2 f_a}\right)} \quad (3)$$

134 where Z is the electrical impedance of the resonators.

135 2.3. 2D FEM Simulations

136 2D simulations are used to study the resonators to reduce computation
 137 time and memory use, which are relatively extensive for 3D simulations,
 138 especially for the combination of small mesh size and large structures. How-
 139 ever, 2D simulations have a limitation that has to be accounted for in order
 140 to make reasonable comparisons between the three design cases. Using 2D
 141 designs implies that the effect of apodization [6], [22] on the resonator per-
 142 formance is not included. Therefore, lateral standing waves caused by Lamb
 143 waves, the so-called spurious modes, strongly affect the electrical responses
 144 of the resonators. The coupling into spurious modes is even more pronounced
 145 as the resonator size shrinks, as reported in previous work [23]. The Q factors
 146 calculated based on the 2D FEM simulation results are very sensitive to these
 147 modes. If they appear in the proximity of f_a , they can alter the slope of the
 148 phase of the electrical impedance, as shown in Fig. 2. This leads to a signifi-
 149 cant drop in Q_a value independent of resonator active area. This phenomenon
 150 occurs in both non-framed and framed FBAR designs. For instance, in the
 151 active region of the non-framed FBAR shown in Fig. 1(a), there exists four
 152 Lamb modes at f_a – two symmetric modes (S_0 , S_1) and two anti-symmetric
 153 modes (A_0 , A_1). According to Fig. 3, the half wavelengths of the A_0 , A_1 , S_0 ,
 154 and S_1 modes at f_a are 735 nm, 1512.5 nm, 902.5 nm, and 1387 nm, respec-
 155 tively. It can be readily calculated that the electrode length $2l = 75 \mu\text{m}$ is
 156 approximately an odd multiple of the S_0 modes half wavelength. It implies
 157 that the spurious mode seen in the vicinity of f_a in Fig. 2 (the dashed line) is

158 the lateral resonance of the S_0 mode. Indeed, Fig. 4 shows a repeating pat-
 159 tern of the Q_a variation for the non-framed FBAR as the length l is varied
 160 for a short range. The local minima of Q_a occur approximately every $1.8 \mu\text{m}$,
 161 which is nearly one wavelength λ_{S_0} of the S_0 mode. This result agrees with

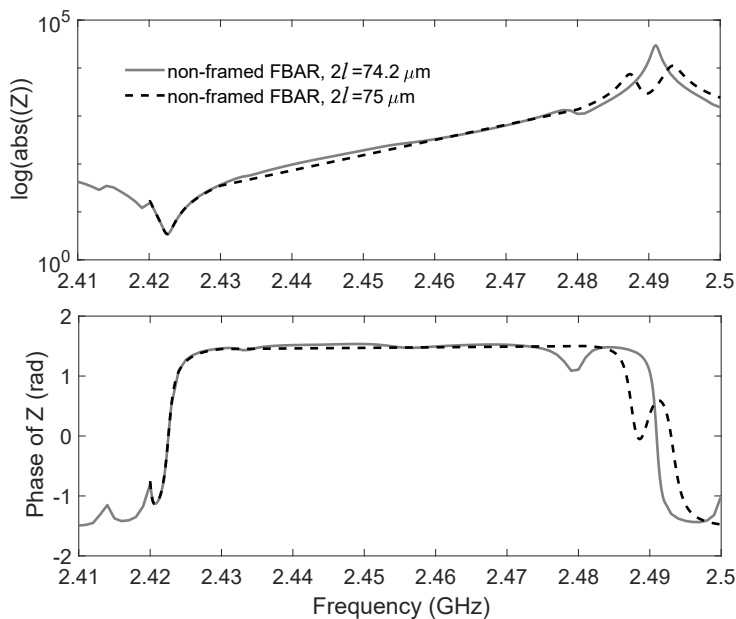


Figure 2: Electrical responses of the FBAR without a frame for two different areas.

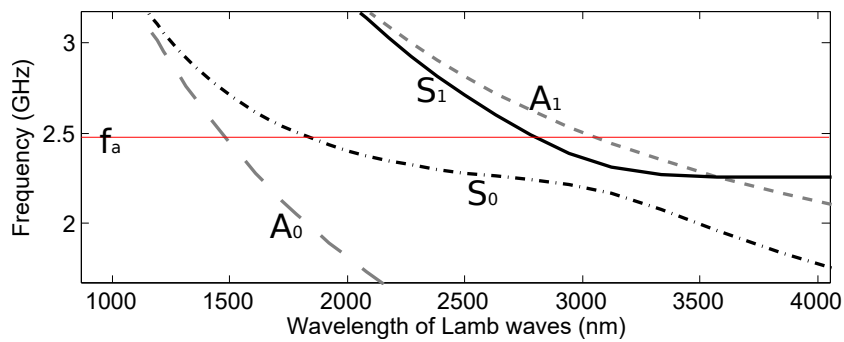


Figure 3: The wavelength of Lamb waves at f_a in the active region of a non-framed FBAR as in Fig. 1(a) with $2l = 75 \mu\text{m}$.

162 the condition for the occurrence of lateral standing S_0 waves, namely

$$2l = (2r + 1) \frac{\lambda_{S_0}}{2} \quad (4)$$

163 where r is a non-negative integer. To avoid the sensitivity of the calculated
 164 Q factors on the spurious modes, in the following simulations, all the l values
 165 of the non-framed FBARs are selected so that the spurious modes do not
 166 occur in the vicinity of f_a . However, in the case of the single and dual step
 167 framed FBARs, the local minima of Q_a occur in a less predictable way. In
 168 order to ensure a fair comparison between the three designs in Fig. 1, a search
 169 is done around each evaluated area of the non-framed active region to find
 170 the area of the framed design that gives the highest Q_a . This results in
 171 a slight difference (about $1\text{--}9\mu\text{m}^2$) between the active areas for the three
 172 design cases at the same point of evaluation, which, is negligible. It has to
 173 be noted that the same phenomenon also happens at resonance frequency as
 174 seen in Fig. 2. However, the spurious modes are densely distributed within
 175 a frequency range near and below f_r especially when the area of the FBARs
 176 increases. Therefore varying l (by very fine steps) is no longer an effective
 177 way in avoiding these modes, except when l is really small and the modes
 178 are sparsely distributed. The mentioned procedure is thus applied only for
 179 avoiding the spurious modes close to f_a .

180 Simulations are also carried out for two different sets of values of the
 181 isotropic mechanical loss factors η_s . The first set is listed in Table 1. For

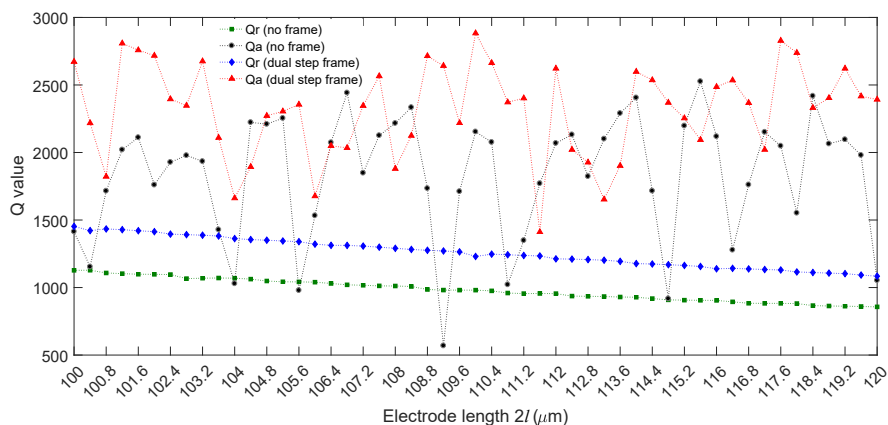


Figure 4: Q_r and Q_a of the two FBAR designs in Fig. 1(a) and (c) for various lengths $2l$ of the top electrode.

182 the second set of values, the mechanical loss factor η_s for AlN is changed to
 183 $1/6000$, i.e. 33% lower than the loss value in the first set. The purpose of
 184 these simulations is to compare the impact of the dual step frame design on
 185 the resonators' performance for the two different material qualities.

186 *2.4. Results and Discussions for the FBARs*

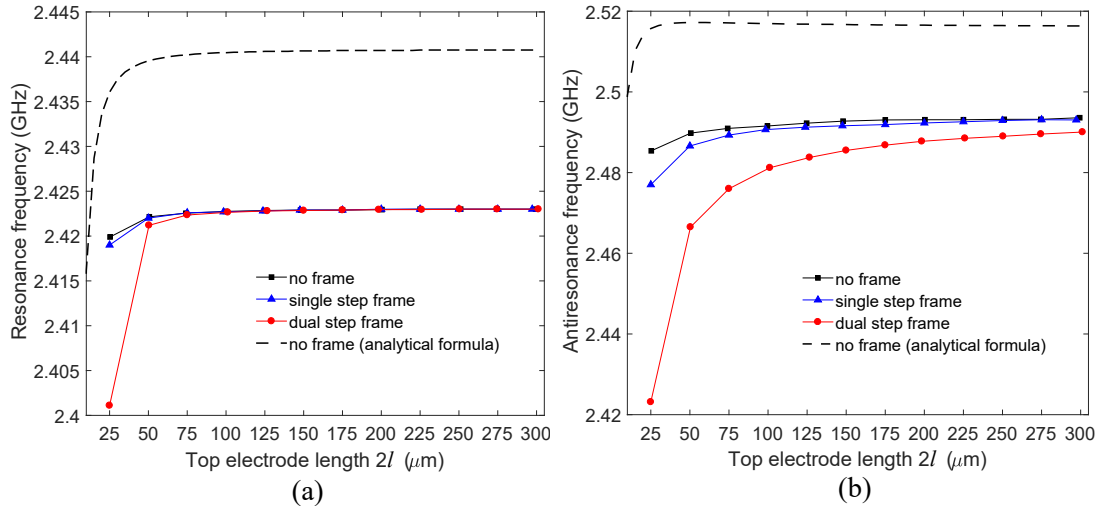


Figure 5: Resonance (a) and antiresonance (b) frequencies versus top electrode length for the three FBAR designs shown in Fig. 1.

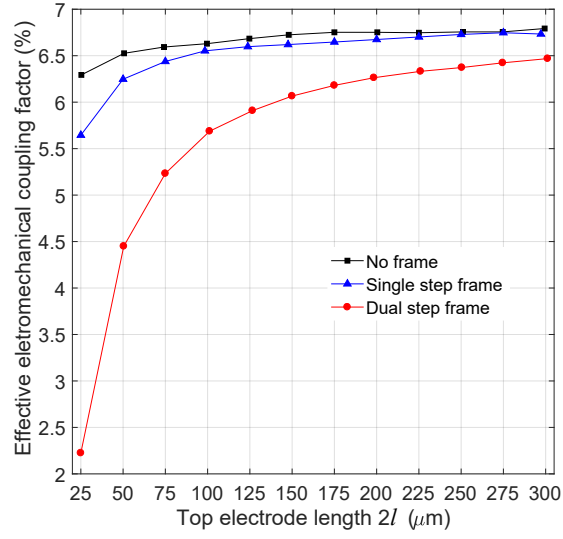


Figure 6: k_{eff}^2 versus top electrode length plotted for the three FBAR designs presented in Fig. 1.

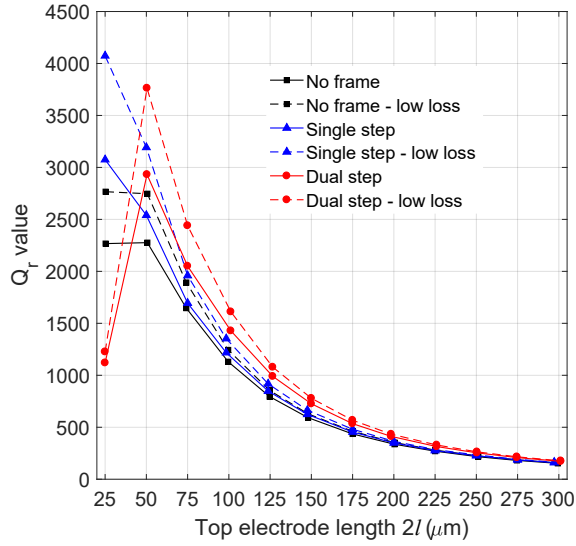


Figure 7: Q_r of the FBAR designs depicted in Fig.1 for two sets of material loss parameters: with material loss parameters obtained from Table 1 (solid lines) and with the mechanical loss factor η_s for AlN set to 1/6000 (dashed lines).

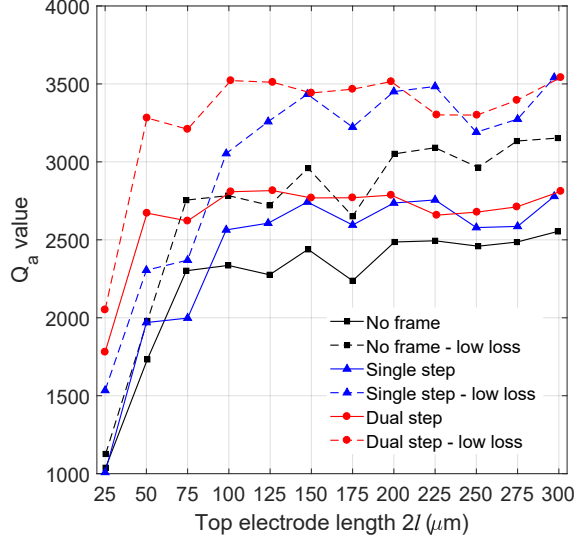


Figure 8: Q_a of the FBAR designs depicted in Fig.1 for two sets of material loss parameters: with material loss parameters obtained from Table 1 (solid lines) and with the mechanical loss factor η_s for AlN set to 1/6000 (dashed lines).

187 Fig. 5, Fig. 6, Fig. 7, and Fig. 8 respectively show the dependence of the
 188 resonance frequency f_r and antiresonance frequency f_a , the electromechanical
 189 coupling factor k_{eff}^2 , the Q_r factor, and the Q_a factor on the top electrode
 190 length, plotted for the three FBAR designs presented in Fig.1. In Fig. 5
 191 and Fig. 6, since the loss factor η_s of AlN does not significantly influence f_r ,
 192 f_a , and k_{eff}^2 , these parameters are plotted only for the set of material loss
 193 parameters in Table 1.

194 In Fig. 5 we see that for all designs, both f_r and f_a reduces from a more or
 195 less stable value when top electrode length decreases. The same trend is seen
 196 if resonance frequency and antiresonance frequency are calculated from (1)
 197 and plotted in Fig. 5 as dotted lines. The analytical formula (1) overestimates
 198 the values by about 1% due to the approximate calculation of the vertical
 199 propagation component for the active region and the simplified boundary
 200 conditions along the electrode edge when the thin plate approximations are
 201 applied. However, the decreasing resonance frequency for decreasing elec-
 202 trode length l is predicted. It can be deduced from (A.9) in the appendix
 203 that a smaller l results in a larger lateral propagation constant which then
 204 combined with (A.13) explains the smaller resonance frequency f_r of the

205 trapped TE_1 mode in the active region compared to the resonance frequency
 206 of the pure TE_1 mode. The maximum value of f_r therefore occurs when the
 207 active region is significantly larger. Then the lateral Lamb mode propaga-
 208 tion constant approaches zero and pure thickness extensional vibration can
 209 be assumed. For the FBAR designs with single step and dual step frames,
 210 the non-framed active areas reduce, making their f_r smaller than that of the
 211 FBAR without frame, especially in the case of the smallest area resonators.

212 The coupling factor k_{eff}^2 increases with resonator area as shown in Fig.
 213 6 since coupling to undesirable spurious modes coexisting in the resonator
 214 is larger for smaller area [24], leading to lower coupling to the main TE_1
 215 mode. In the worst case of FBAR with dual step frame where the active
 216 area is $25 \times 25 \mu\text{m}^2$, the resonator provides quite poor coupling. The reason
 217 is that part of the energy is shared with the vibration of the frame regions,
 218 which have relatively large areas compared to the non-framed active area
 219 ($\approx 563 \mu\text{m}^2$ to $62 \mu\text{m}^2$). These frame steps can be considered as “parasitic
 220 resonators” in parallel with the main resonator. They resonate at lower fre-
 221 quencies than the main resonance frequency due to additional electrode mass
 222 loading. It means the electromechanical coupling in the dual step framed
 223 FBAR is not as high as in the case of a non-framed or a single step frame
 224 FBAR. Note that the framed to non-framed active area ratio for the single
 225 step frame FBAR is only $140 \mu\text{m}^2 / 485 \mu\text{m}^2$. This low k_{eff}^2 value leads to a
 226 large downward shift of f_a compared to those of the other two FBAR designs
 227 of the same size, as shown in Fig. 5(b).

228 In Fig. 7, Q_r for all designs decreases as l increases, except for the lowest
 229 value of l in the case of the dual step framed FBAR. The resonators with
 230 relatively small l values are less affected by the ohmic loss, formulated as
 231 $R_s |I|^2$, leading to higher Q_r . This is reasonable since the amplitude of the
 232 current running through the electrodes, which peaks at f_r , increases with
 233 l (and hence Z decreases with resonator area) as described in (A.18) for
 234 the non-framed FBAR case. The worst case of the dual step frame FBAR
 235 may be due to the dominance of motional loss, occurring when f_r and k_{eff}^2
 236 significantly reduce [25]. For the same area, the dual step frame FBAR design
 237 in Fig. 1(c) provides the largest Q_r values due to the reduced resistance in the
 238 frame region. This advantage gradually diminishes as l increases. For larger
 239 active areas, the current becomes so large that ohmic loss strongly dominates
 240 and the contribution of a frame is negligible. In contrast to Q_r , Q_a values
 241 for all three designs tend to increase when l increases as seen in Fig. 8. This
 242 can qualitatively be explained by the contribution of the lateral leakage to

243 the total loss in the resonators. The total stored energy of the resonators are
 244 proportional to their areas whilst the lateral leakage is proportional to their
 245 peripheries. A bigger resonator always has a larger area to periphery ratio,
 246 hence larger stored energy to lateral power loss ratio, i.e. larger $Q_a^{lateral}$.
 247 The total Q_a is also influenced by other factors, like Q_a^{mech} due to material
 248 viscosity and $Q_a^{dielectric}$ due to dielectric loss, which can be expressed as

$$\frac{1}{Q_a} = \frac{1}{Q_a^{lateral}} + \frac{1}{Q_a^{mech}} + \frac{1}{Q_a^{dielectric}} \quad (5)$$

249 For smaller active area, the lateral leakage is the dominant loss mechanism
 250 and Q_a follows $Q_a^{lateral}$. However, when the active area increases, $Q_a^{lateral}$
 251 increases to a point where the other losses start to dominate and Q_a fol-
 252 lows Q_a^{mech} and/or $Q_a^{dielectric}$ which are independent of electrode length $2l$.
 253 It means Q_a of each resonator design experiences less drastic change and
 254 becomes stable as l continues increasing.

255 Fig. 8 shows a significant improvement of Q_a that the dual step frame
 256 FBAR offers in comparison with the non-framed and the single step frame
 257 FBARs, for electrode lengths up to 125 μm . Selecting which design to im-
 258 plement in a filter will then become a trade-off between the coupling factor
 259 requirements and the need for high quality factors. For those applications
 260 where small resonator area in combination with very high Q are the most
 261 critical, the dual step frame design may be the most promising candidate
 262 compared to other designs. For wideband applications, if piezoelectric mate-
 263 rials with larger intrinsic coupling coefficient, e.g. single crystalline or doped
 264 AlN [26], [27], the dual step frame FBAR could still be applicable.

265 Fig. 7 and Fig. 8 show that the use of a better quality AlN film can help
 266 improve the effectiveness of the dual step frame design in increasing the Q
 267 factors of smaller size FBARs. The benefit of high material quality factor
 268 on the resonator Q_r , however, diminishes as the resonator area reaches
 269 $200 \times 200 \mu\text{m}^2$ due to the dominance of ohmic loss though it is not the case
 270 for Q_a .

271 Fig. 9 compares the total power loss in the outside regions at antireso-
 272 nance frequency for the three resonator designs. This loss is calculated from
 273 the total acoustic Poynting vector for piezoelectric materials using the FEM
 274 simulation software and is normalized to the maximum obtained loss value.
 275 In general, the power dissipation to the outside region of the dual step frame
 276 FBAR is less than those of the other two designs of the same size. This

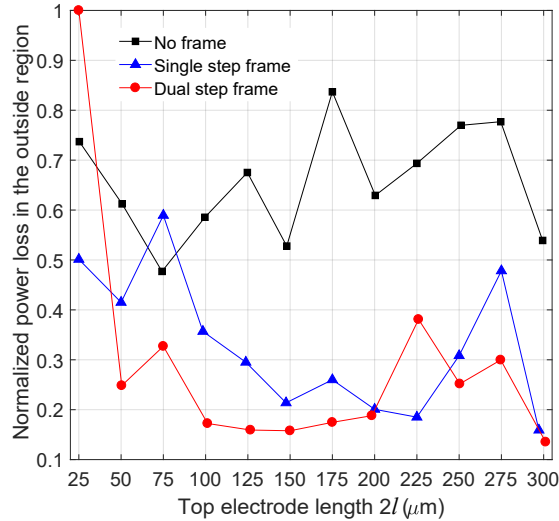


Figure 9: Normalized power loss to the outside region at f_a , plotted for the various FBAR designs shown in Fig. 1.

277 confirms the benefit of a dual step frame design in alleviating the laterally
 278 leaking of acoustic energy.

279 3. SMR

280 3.1. Design and Modeling

281 The SMR is a stratified structure consisting of three main parts. The
 282 first one, called the resonating part, is a piezoelectric thin film sandwiched
 283 between two metal electrodes. The fundamental longitudinal waves (TE_1)
 284 are vertically confined in this three-layered stack, forming a standing wave
 285 and thus the main resonance. Below this stack is placed an acoustic Bragg
 286 mirror that comprises of alternate high and low acoustic impedance layers.
 287 The purpose of this mirror is to enhance reflection of the acoustic waves,
 288 so the energy loss into the third part – the substrate below the mirror – is
 289 diminished.

290 In this paper, the SMR is designed to resonate at approximately 2.30 GHz
 291 with the antiresonance being at about 2.36 GHz for $100 \times 100 \mu\text{m}^2$ resonator
 292 area. The SMR geometry with thicknesses and materials of all layers is
 293 illustrated in Fig. 10(a). All the layers are assumed to be homogeneous
 294 and perfectly flat. The mirror of the designed SMR comprises of 4 layers

295 of SiO_2 and 3 layers of Ir alternately stacked together. Ir is chosen for both
 296 electrodes and the mirror instead of W as it offers higher acoustic impedance,
 297 better conductivity, and better adhesion to the SiO_2 layers in the mirror. The
 298 high compressive residual stress in magnetron sputtered W films can cause
 299 buckling and delamination [28] in this multilayer structure. In addition, the
 300 large ratio between the acoustic impedance of Ir and SiO_2 ensures a good
 301 reflectivity for the mirror. In the resonating part of the SMR, although TE_1
 302 is the main mode, thickness shear waves are also excited and if they are
 303 not well-confined, they will propagate through the mirror into the substrate
 304 significantly degrading the Q factors even if the energy associated with these
 305 waves is small [13]. It is therefore essential to design the mirror that is able to
 306 reflect both longitudinal and shear waves at the operating frequencies f_r and
 307 f_a . With the mirror configuration shown in Fig. 10 and material properties
 308 listed in Table 1, the transmission curves of the two wave modes are plotted
 309 in Fig. 11. From the figure, it can be observed that the mirror provides a
 310 good reflectivity for both TE_1 and TS_1 modes at f_r and f_a .

311 For an SMR, the inhibition of acoustic leakage in the lateral direction is
 312 as important as for the vertical direction in order to achieve high Q factors,
 313 so a dual step frame working as a lateral Bragg mirror is placed at the edge

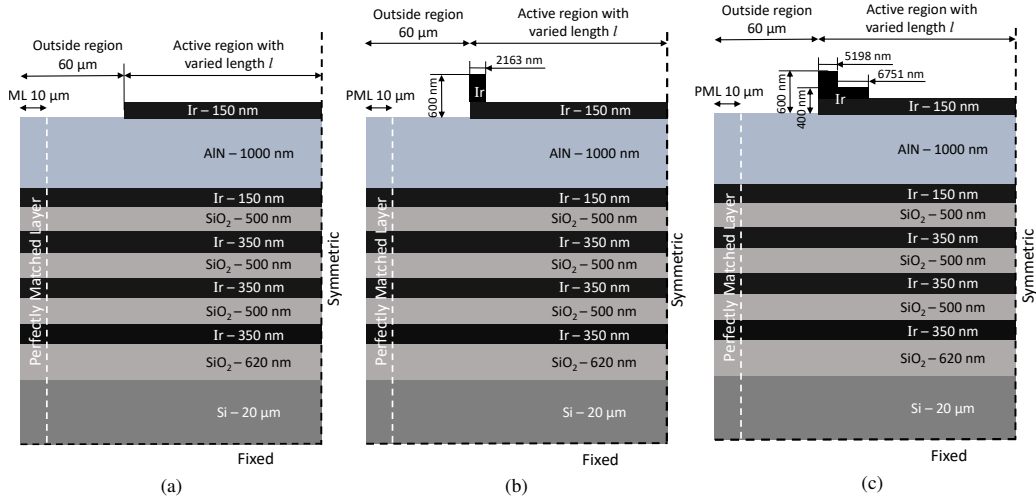


Figure 10: 2D schematics of the simulated SMR designs without frame (a), with a single frame (b), and with a dual step frame (c). The resonators are not drawn to scale. The value of l ranges from around 30 to 150 μm .

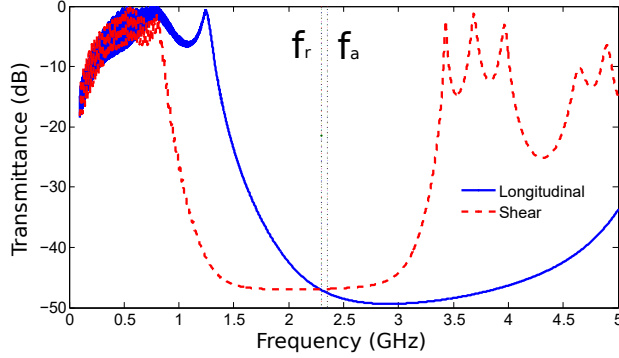


Figure 11: The transmittance of the mirror that has the SiO₂–Ir configuration shown in Fig. 10.

314 of the active region as in the case of the FBAR. The purpose of this frame
 315 is to reflect the two propagating plate modes M_4 and M_5 at f_a as labeled in
 316 Fig. 12. This dispersion diagram is obtained by taking the discrete Fourier
 317 transform of the vertical displacement component at the surface of the top
 318 electrode extracted from FEM simulations. Due to the highly asymmetric
 319 semi-infinite SMR structure, Lamb modes can no longer be categorized as
 320 symmetric and antisymmetric modes. They are instead called generalized
 321 Lamb waves labeled M_i , which have more complicated behavior than the
 322 standard Lamb waves [29]. As in the FBAR case, the frame should reflect
 323 the two modes that have the largest power, determined by using Poynting's
 324 theorem [10]. However, the power analysis for these plate modes are much
 325 more complicated in the case of SMR-type BAW resonators and are not
 326 carried out in the present paper. Modes M_4 and M_5 are therefore selected
 327 since they have the largest velocities among the plate waves and share some
 328 similar traits with the two modes S_1 and A_1 in the non-framed FBAR case.
 329 In Fig. 12, the left branch of mode M_5 has negative slope and its cut-off
 330 frequency is at the resonance frequency of the trapped TE_1 mode. The mode
 331 M_4 has cut-off frequency at the resonance frequency of the trapped thickness
 332 shear mode, similar to the A_1 mode.

333 The frame is designed by finding the wavelengths λ_{M_4} and λ_{M_5} of the
 334 M_4 and M_5 modes in the two step regions, and they have to approximately
 335 satisfy the equation

$$(2p + 1) \frac{\lambda_{M_4}}{4} = (2q + 1) \frac{\lambda_{M_5}}{4} \quad (6)$$

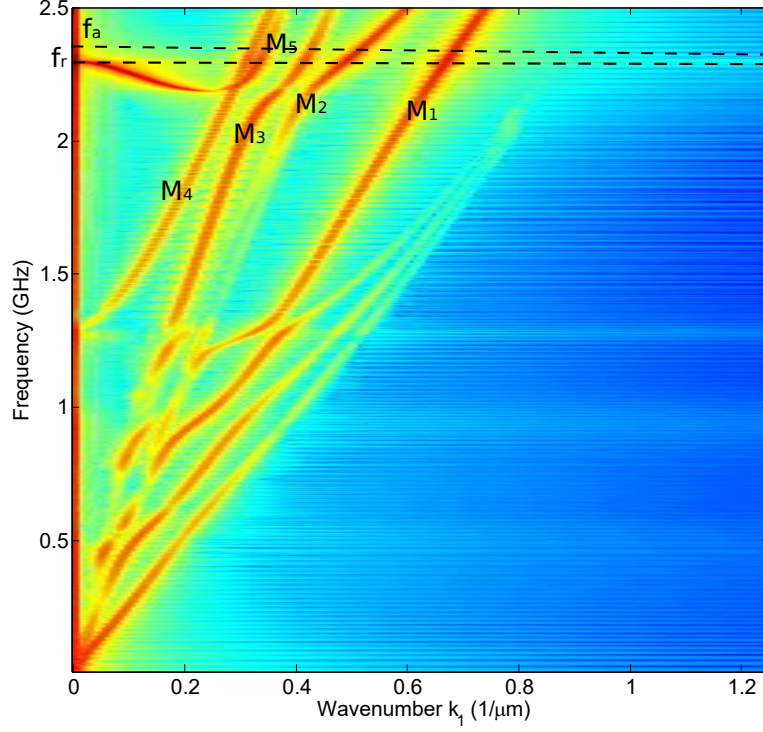


Figure 12: Dispersion diagram for the active region of the SMR without a frame [Fig. 10 (a)].

336 where p and q are non-negative integers. As the thickness of the top Ir layer
 337 increases, the dispersion of the plate waves changes. The wavelengths of the
 338 modes $M_{4,5}$ at f_a are respectively 2439 nm and 3000 nm for the step region
 339 of 400 nm high, and are 2344 nm and 2970 nm for the step region of 600 nm
 340 high. The resulting (p, q) pairs for the 400 nm-height step is thus (5, 4) and for
 341 the 600 nm-height step is (4, 3). The dimensions of the calculated dual step
 342 frame SMR is shown in Fig. 10 (c). The single step frame SMR design, whose
 343 step width equals three quarter wavelength of the mode M_5 , as depicted in
 344 Fig. 10(b), is also simulated. The area of the active regions does not change
 345 when the frame is added. The length l ranges from 30 μm to 150 μm . Smaller
 346 values of l are not shown due to the considerably poor coupling factor in the
 347 resonators. All the simulated SMRs are square resonators which areas are
 348 $2l \times 2l$. As in the FBAR cases, l values are also selected so that the spurious
 349 modes occurring near f_a are avoided and the calculated Q_a factors are those

350 least influenced by these modes.

351 As in the case of FBAR, the influence of material losses on the effec-
 352 tiveness of the dual step frame design is investigated. The simulations for
 353 the SMR designs are thus carried out for two different sets of values of the
 354 isotropic mechanical loss factors η_s . The first set of values are those obtained
 355 from Table 1. For the second set, η_s of AlN, SiO₂, and Ir are set to 1/6000,
 356 1/2000, and 1/1000 respectively. It means a reduction of 33%, 41%, and 70%
 357 relative to the loss values listed in Table 1.

358 *3.2. Simulation Results for the SMRs*

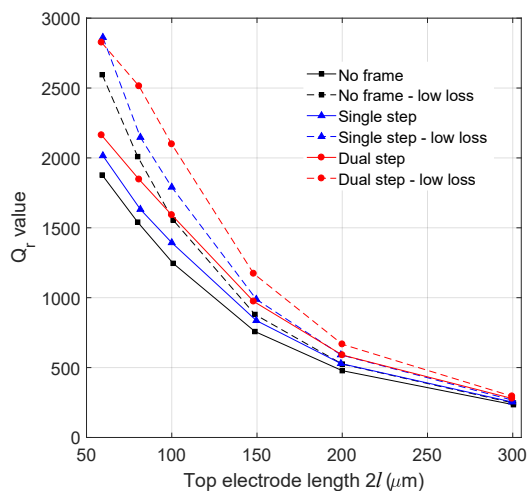


Figure 13: Q_r of the SMR designs shown in Fig. 10 with material loss parameters obtained from Table 1 (solid lines) and low material losses (dashed lines).

359 Fig. 13 and Fig. 14 show Q_r and Q_a of the three SMR designs in Fig. 10
 360 with various sets of loss parameters. As pointed out previously, the Q_r factor
 361 of the resonator decreases with size for all designs. For the same active area,
 362 the SMR with a dual step frame design gives marginally higher Q_r due to
 363 lower ohmic loss. However, this difference decreases with increasing electrode
 364 length. For most of the values of active area, Q_a is higher in the case of dual
 365 step frame SMR than for the other two cases.

366 Compared to a non-framed SMR, an SMR with a dual step frame and
 367 with the use of high quality materials offers potentially higher Q factors at
 368 both f_r and f_a when its size decreases. More specially, when material losses
 369 are reduced, compared to other designs, there is a larger improvement in

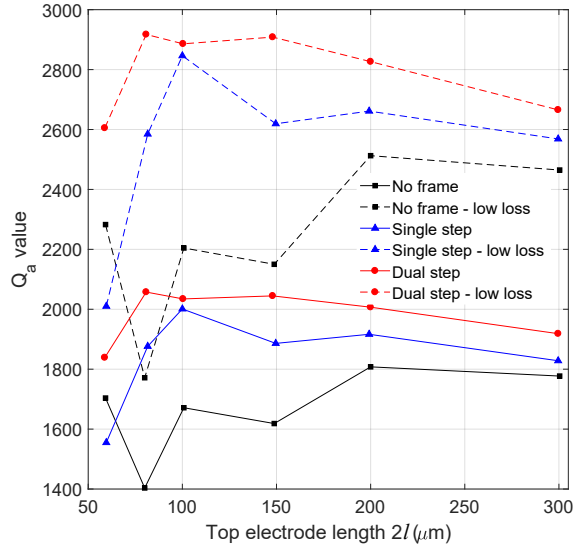


Figure 14: Q_a of the SMR designs shown in Fig. 10 with material loss parameters obtained from Table 1 (solid lines) and low material losses (dashed lines).

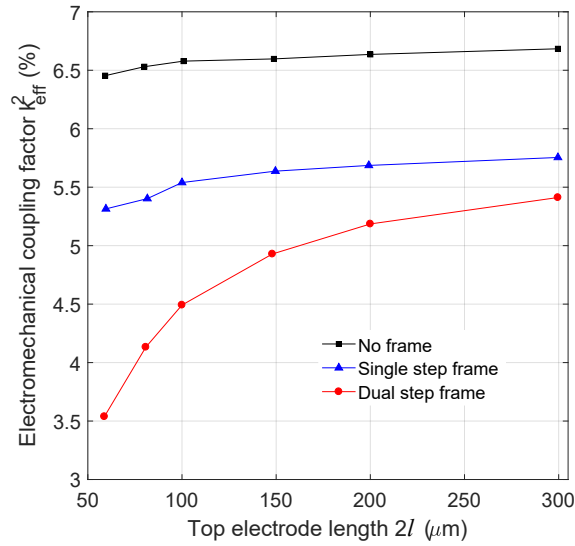


Figure 15: k_{eff}^2 of the three SMR designs depicted in Fig. 10.

370 both Q_r and Q_a of the dual step frame SMR than the improvement obtained

371 with material losses in Table 1. In addition, this improvement is even more
372 pronounced as the resonator area decreases. However, the use of a dual step
373 design comes with the decline of k_{eff}^2 as shown in Fig. 15. This reduction is
374 more distinct than it is for the dual step frame FBAR due to the increased
375 frame area. Since f_r and f_a are not significantly affected by the loss of the
376 used materials, the k_{eff}^2 shown in Fig. 15 is applicable for both set of material
377 parameters.

378 4. Conclusions

379 The area has immense impact on the performance of the BAW resonators.
380 The coupling to spurious modes can be strong at resonance and/or antireso-
381 nance frequencies for some specific sizes of resonator areas, causing massive
382 degradation of the Q factors. In designing the BAW resonator, it is thus
383 essentially to avoid these values by using the lateral resonance condition for
384 Lamb modes at the frequencies of interest. The Q_r factor of the resonator
385 increases rapidly as the resonator area is miniaturized. The dual step frame
386 designs significantly improve this Q_r factor compared to those of the non-
387 frame and single step frame resonators of the same size, especially for small
388 area resonators. However, this improvement diminishes as the resonator area
389 increases due to the large influence of ohmic loss on the electrical characteris-
390 tic. The utilization of the dual step frame, more importantly, helps improve
391 the Q_a factors of the miniaturized non-framed resonators. However, the elec-
392 tromechanical coupling factors of these dual-step-framed resonators reduce
393 as a trade-off. The obtained simulation results also show that the better ma-
394 terial quality, the more effective the dual step frame design is in improving
395 the resonator quality factors.

396

397 Acknowledgement

398

399 This work was supported in part by the University of Oslo and in part
400 by the Norwegian Metacenter for High Performance Computing under Grant
401 NN9344K.

402 The authors would like to thank Prof. Enrique Iborra and his group at
403 the Technical University of Madrid for providing the software used in design-
404 ing the acoustic mirror for the simulated SMRs.

405

406 References

407

- 408 [1] R. Ruby, A Snapshot in Time: The Future in Filters for Cell Phones,
409 IEEE Microwave Magazine 16 (2015) 46–59.
- 410 [2] S. Sethi, FBAR gets excellent reception, Technical Report 11440, The
411 Linley Group, 2015.
- 412 [3] P. Warder, A. Link, Golden Age for Filter Design: Innovative and
413 Proven Approaches for Acoustic Filter, Duplexer, and Multiplexer De-
414 sign, IEEE Microwave Magazine 16 (2015) 60–72.
- 415 [4] K. Hashimoto, T. Kimura, T. Matsumura, H. Hirano, M. Kadota,
416 M. Esashi, S. Tanaka, Moving Tunable Filters Forward: A "Heteroin-
417 tegration" Research Project for Tunable Filters Combining MEMS and
418 RF SAW/BAW Technologies, IEEE Microwave Magazine 16 (2015) 89–
419 97.
- 420 [5] R. Aigner, Tunable Filters? Reality Check Foreseeable Trends in System
421 Architecture for Tunable RF Filters, IEEE Microwave Magazine 16
422 (2015) 82–88.
- 423 [6] K. Hashimoto (Ed.), RF bulk acoustic wave filters for communications,
424 Artech House, 2009.
- 425 [7] R. Thalhammer, R. Aigner, Energy loss mechanisms in SMR-type BAW
426 devices, in: IEEE MTT-S International Microwave Symposium Digest,
427 2005.
- 428 [8] C. Muller, M. A. Dubois, Effect of size and shape on the performances
429 of BAW resonators: A model and its applications, in: 2008 IEEE Ul-
430 trasonics Symposium, pp. 1552–1556.
- 431 [9] R. Aigner, S. Marksteiner, L. Elbrecht, W. Nessler, RF-filters in mobile
432 phone applications, in: TRANSDUCERS, Solid-State Sensors, Actu-
433 ators and Microsystems, 12th International Conference on, 2003, vol-
434 ume 1, pp. 891–894.
- 435 [10] N. Nguyen, A. Johannessen, S. Rooth, U. Hanke, A design approach for
436 high-q fbars with a dual-step frame, IEEE Transactions on Ultrasonics,
437 Ferroelectrics, and Frequency Control 65 (2018) 1717–1725.

- 438 [11] N. Nguyen, A. Johannessen, U. Hanke, Design of high-Q Thin Film
439 Bulk Acoustic resonator using dual-mode reflection, in: 2014 IEEE
440 International Ultrasonics Symposium, pp. 487–490.
- 441 [12] X. Li, J. Bao, Y. Huang, B. Zhang, G. Tang, T. Omori, K. y. Hashimoto,
442 Use of double-raised-border structure for quality factor enhancement of
443 type II piston mode FBAR, in: 2017 Joint Conference of the European
444 Frequency and Time Forum and IEEE International Frequency Control
445 Symposium (EFTF/IFCS), pp. 547–550.
- 446 [13] S. Marksteiner, J. Kaitila, G. G. Fattinger, R. Aigner, Optimization
447 of acoustic mirrors for solidly mounted BAW resonators, in: IEEE
448 Ultrasonics Symposium, 2005., volume 1, pp. 329–332.
- 449 [14] H. Tiersten, Linear piezoelectric plate vibrations: elements of the lin-
450 ear theory of piezoelectricity and the vibrations of piezoelectric plates,
451 Plenum Press, 1969.
- 452 [15] H. F. Tiersten, D. S. Stevens, An analysis of thickness-extensional
453 trapped energy resonant device structures with rectangular electrodes
454 in the piezoelectric thin film on silicon configuration, Journal of Applied
455 Physics 54 (1983) 5893–5910.
- 456 [16] R. K. Thalhammer, J. D. Larson, Finite-Element Analysis of Bulk-
457 Acoustic-Wave Devices: A Review of Model Setup and Applications,
458 IEEE Transactions on Ultrasonics, Ferroelectrics, and Frequency Con-
459 trol 63 (2016) 1624–1635.
- 460 [17] J. G. Gualtieri, J. A. Kosinski, A. Ballato, Piezoelectric materials for
461 acoustic wave applications, IEEE Transactions on Ultrasonics, Ferro-
462 electrics, and Frequency Control 41 (1994) 53–59.
- 463 [18] G. Wingqvist, F. Tasndi, A. Zukauskaite, J. Birch, H. Arwin, L. Hult-
464 man, Increased electromechanical coupling in w- $\text{Sc}_x\text{Al}_{1-x}\text{N}$, Applied
465 Physics Letters 97 (2010).
- 466 [19] P. Muralt, J. Antifakos, M. Cantoni, R. Lanz, F. Martin, Is there a
467 better material for thin film BAW applications than AlN?, in: IEEE
468 Ultrasonics Symposium, 2005., volume 1, pp. 315–320.

- 469 [20] Y. Zhang, D. Chen, Multilayer Integrated Film Bulk Acoustic Resonators, Springer-Verlag Berlin Heidelberg, 2013.
470
- 471 [21] Private conversations with Enrique Iborra, UPM, Spain, 2016.
- 472 [22] R. Ruby, J. Larson, J. Feng, S. Fazio, The effect of perimeter geometry on FBAR resonator electrical performance, in: IEEE MTT-S International Microwave Symposium Digest, 2005.
473
474
- 475 [23] T. Pensala, M. Ylilammi, J. Meltaus, K. Kokkonen, P2g-5 Area and Dispersion Dependence of Vibration Shape and Coupling Coefficient in Thin Film BAW Resonators, in: 2007 IEEE Ultrasonics Symposium Proceedings, pp. 1661–1664.
476
477
478
- 479 [24] T. Pensala, M. Ylilammi, Spurious Resonance Suppression in Gigahertz-Range ZnO Thin-Film Bulk Acoustic Wave Resonators by the Boundary Frame Method: Modeling and Experiment, IEEE Transactions on Ultrasonics, Ferroelectrics, and Frequency Control 56 (2009) 1731–1744.
480
481
482
- 483 [25] H. Campanella, Acoustic Wave and Electromechanical Resonators, Artech House, 2010.
484
- 485 [26] J. B. Shealy, J. B. Shealy, P. Patel, M. D. Hodge, R. Vetury, J. R. Shealy, Single crystal aluminum nitride film bulk acoustic resonators, in: 2016 IEEE Radio and Wireless Symposium (RWS), pp. 16–19.
486
487
- 488 [27] T. Yokoyama, Y. Iwazaki, Y. Onda, Y. Sasajima, T. Nishihara, M. Ueda, Highly piezoelectric co-doped AlN thin films for wideband FBAR applications, in: 2014 IEEE International Ultrasonics Symposium, pp. 281–288.
489
490
491
- 492 [28] P. Waters, A. A. Volinsky, Stress and Moisture Effects on Thin Film Buckling Delamination, Experimental Mechanics 47 (2007) 163–170.
493
- 494 [29] B. A. Auld, Acoustic waves and fields in solids, volume 2, John Wiley and Sons, New York, 1973, pp. 97–102.
495

496 **Appendix A.**

497 Following the approach in [15] in which the structure in Fig. A.1 (a) was
 498 studied, we analyze the one shown in Fig. A.1 (b) with the specified material
 499 parameters. Compared to the analyzed structure in [15], in our analysis,
 500 a tungsten layer of thickness h^w replaces the silicon layer under the bottom
 501 electrode and the bottom electrode thickness h'' is set to zero. This difference
 502 does not change the boundary conditions at the layer interfaces and free
 503 surfaces in the active or outside regions.

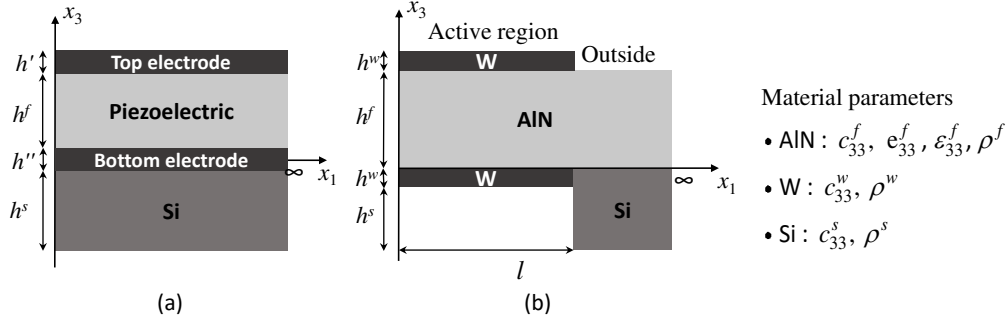


Figure A.1: The analyzed structure used in [15] (a) and half of the analyzed FBAR structure (b).

504 The electrical potential inside AlN and the vertical displacement fields for
 505 the trapped thickness-extensional mode n in x_3 direction in the AlN, Si and
 506 bottom W layers in the active region when a harmonic bias with amplitude
 507 V is applied between the top and bottom electrode are of the forms

$$\bar{u}_3^{fn}(x_1, x_3, t) = (A^n \cos(\eta_n x_3) + B^n \sin(\eta_n x_3)) f^n(x_1, t) - \frac{e_{33}^f V x_3}{c_{33}^f h^f} e^{j\omega t}, \quad (\text{A.1})$$

$$\bar{\varphi}^{fn}(x_1, x_3, t) = \frac{e_{33}^f}{\varepsilon_{33}^f} (A^n \cos(\eta_n x_3) + B^n \sin(\eta_n x_3)) f^n(x_1, t) + \left(C x_3 + K + \frac{V x_3}{h^f} \right) e^{j\omega t}. \quad (\text{A.2})$$

509 The x_3 dependency is governed by pure standing thickness-extensional waves
 510 and the constants A^n , B^n , and the propagation constant η_n for each layer
 511 can be determined by applying the boundary conditions of zero stress at the

512 surfaces and continuity of fields at the interfaces. The constants C and K
 513 are determined by the electrical boundary conditions at the top and bottom
 514 electrodes. The vertical displacement field in the AlN layer in the outside
 515 region has the same form but with bias V set to zero. For the Si film, the
 516 second term in (A.1) and the potential field in (A.2) both vanish.

517 In the active region the propagation constant $\eta_n = \bar{\eta}_{nf}$ inside the AlN
 518 film in the vertical x_3 direction is found by solving

$$\begin{aligned}
 & -2 + \frac{\eta}{k^2} \sin \eta + 2 \cos \eta + 2 \frac{c^r \mu \eta}{k^2} \cos \eta \tan(\mu \sigma \eta) - c^r \mu \tan(\mu \sigma \eta) \sin \eta + \\
 & + R' \left[\frac{\eta^2}{k^2} \cos \eta - \eta \sin \eta - \frac{\eta}{k^2} c^r \mu \eta \sin \eta \tan(\mu \sigma \eta) \right] = 0
 \end{aligned} \tag{A.3}$$

519 in which $\eta = \bar{\eta}_{nf} h^f$, $k^2 = \left(e_{33}^f \right)^2 / \left(\bar{c}_{33}^f \varepsilon_{33}^f \right) = \hat{k}^2 / \left(\hat{k}^2 + 1 \right)$, $c^r = c_{33}^w / \bar{c}_{33}^f$,
 520 $\bar{c}_{33}^f = c_{33}^f + (e_{33}^f)^2 / \varepsilon_{33}^f$, $\mu = \sqrt{\left(\bar{c}_{33}^f \rho^w \right) / c_{33}^w \rho^f}$, $R' = \rho^w h^w / \rho^f h^f$ and $\sigma =$
 521 h^w / h^f . All the quantities denoted with a bar on top indicates that these
 522 quantities are calculated for the active region except for \bar{c}_{33}^f . Further, the
 523 resonance frequency for the n^{th} pure thickness-extensional wave is then found
 524 from

$$\bar{\omega}_e = \sqrt{\frac{\bar{c}_{33}^f}{\rho^f} \bar{\eta}_{nf}}. \tag{A.4}$$

525 Similarly, in the outside region, the propagation constant $\eta_n = \eta_{out,n}$ inside
 526 the AlN film in the vertical x_3 direction is calculated from

$$\tan(\eta_{out,n} h^f) + c_{out}^r \mu_{out} \tan(\mu_{out} \sigma_{out} \eta_{out,n} h^f) = 0 \tag{A.5}$$

527 where $c_{out}^r = c_{33}^s / \bar{c}_{33}^f$, $\mu_{out} = \sqrt{\left(\bar{c}_{33}^f \rho^s \right) / c_{33}^s \rho^f}$, and $\sigma_{out} = h^s / h^f$. The
 528 resonance frequency for the pure thickness-extensional wave in the outside
 529 region is found from

$$\omega_e^{out} = \sqrt{\frac{\bar{c}_{33}^f}{\rho^f} \eta_{out,n}}. \tag{A.6}$$

530 The mode shape function in the active region $f^n(x_1, t)$ can be shown to fulfill

531 the inhomogeneous partial differential equation

$$M_n \frac{\partial^2 f^n}{\partial x_1^2} - \bar{c}_{33}^f \eta_{fn}^2 f^n - \rho^f \frac{\partial^2 f^n}{\partial t^2} = \rho^f \omega^2 \frac{e_{33}^f}{c_{33}^f} \frac{G_1^n}{h^f G_2^n} V e^{j\omega t}, \quad (\text{A.7})$$

532 in which expressions for M_n , G_1^n , and G_2^n can be found in [15]. The mode
533 shape function in the outside region is the solution of a similar partial dif-
534 ferential equation with zero bias voltage and material parameters changed
535 accordingly.

536 We first find solutions of the homogeneous partial differential equation
537 obtained when the bias voltage is set to zero in (A.7). Assuming propagating
538 waves in the active region and a decaying wave on the outside we can write
539 the solutions $f^n(x_1, t)$ to the homogeneous equation for the active and outside
540 regions as

$$f_\mu^n(x_1, t) = \begin{cases} \bar{f}_\mu^n = \bar{E}_n \cos(\bar{\xi}_{n\mu} x_1) e^{i\omega t}, & x_1 \leq l \\ f_\mu^{out,n} = \bar{E}_n \cos(\bar{\xi}_{n\mu} l) e^{-\xi_{out,n\mu}(x_1-l)} e^{i\omega t}, & l < x_1 < \infty. \end{cases} \quad (\text{A.8})$$

541 The index μ now refers to the order of the lateral resonance mode. It is
542 shown in [14] that for thin piezoelectric plates the boundary conditions at
543 the border between the active and outside regions reduces to the continuity
544 of vertical displacements and their first order derivatives. This translates to
545 the continuity of $f^n(x_1, t)$ and its first order derivative. Applying these ap-
546 proximate boundary conditions results in the condition for lateral resonance
547 to occur

$$\bar{\xi}_{n\mu} \tan(\bar{\xi}_{n\mu} l) = \xi_{out,n\mu} \quad (\text{A.9})$$

548 where l is half the electrode length. The dispersion relation for the active
549 region determining the propagation constant $\bar{\xi}_{n\mu}$ in x_1 direction can to the
550 lowest order be written as

$$-\bar{M}_n \bar{\xi}_{n\mu}^2 - \bar{c}_{33}^f \bar{\eta}_{nf}^2 + \rho^f \omega^2 = 0 \quad (\text{A.10})$$

551 in which \bar{M}_n is the value of M_n in the active region. The decay constant
552 $\xi_{out,n\mu}$ is to second order determined from

$$M_{out,n} \xi_{out,n\mu}^2 - \bar{c}_{33}^f \eta_{out,n}^2 + \rho^f \omega^2 = 0 \quad (\text{A.11})$$

553 where $M_{out,n}$ is the value of M_n in the outside region. From A.10 and A.11,
554 we have

$$\xi_{out,n\mu} = \sqrt{\frac{\bar{c}_{33}^f}{M_{out,n}} (\eta_{out,n}^2 - \bar{\eta}_{nf}^2) - \frac{\bar{M}_n}{M_{out,n}} \bar{\xi}_{n\mu}^2}. \quad (\text{A.12})$$

555 The lateral resonance frequency of the trapped TE_n mode is now found by
 556 substituting solutions of (A.9) into (A.10)

$$\omega_{n\mu} = \sqrt{\frac{1}{\rho^f} \left(\overline{M}_n \overline{\xi}_{n\mu}^2 + \overline{c}_{33}^f \overline{\eta}_{nf}^2 \right)} = \sqrt{\overline{\omega}_e^2 + \frac{\overline{M}_n \overline{\xi}_{n\mu}^2}{\rho^f}}. \quad (\text{A.13})$$

557 Material parameters and layer thicknesses used in this work ensures that
 558 the thin plate approximation is valid and that $\xi_{out,n\mu}$ is real and positive.
 559 For these layer thicknesses and material parameters \overline{M}_n is negative, so the
 560 trapped TE_n mode resonates at a lower frequency than the pure TE_n mode.
 561 Now we can use the mode shape functions obtained in the homogeneous case
 562 to find solutions of the inhomogeneous equation (A.7) by a linear combination
 563 of them on the form

$$\begin{aligned} \overline{f}^n &= \sum_{\mu} H^{n\mu} \overline{f}_{\mu}^n, \quad x_1 \leq l \\ f^{out,n} &= \sum_{\mu} H^{n\mu} f_{\mu}^{out,n}, \quad l < x_1 < \infty \end{aligned} \quad (\text{A.14})$$

564 where \overline{f}_{μ}^n and $f_{\mu}^{out,n}$ take the forms in (A.8). Substituting (A.14) into (A.7)
 565 and using (A.13) give

$$\begin{aligned} \sum_{\mu} (\omega^2 - \omega_{n\mu}^2) H^{n\mu} \overline{f}_{\mu}^n &= \omega^2 \frac{e_{33}^f}{c_{33}^f} \frac{G_1^n}{h^f G_2^n} V, \quad x_1 \leq l \\ \sum_{\mu} (\omega^2 - \omega_{n\mu}^2) H^{n\mu} f_{\mu}^{out,n} &= 0, \quad l < x_1 < \infty. \end{aligned} \quad (\text{A.15})$$

566 Multiplying with \overline{f}_{ν}^m and $f_{\nu}^{out,m}$ respectively in (A.15) and applying that the
 567 mode shape functions to a good approximation are orthogonal leads to

$$H^{n\mu} = \frac{2e_{33}^f V G_1^n \sin(\overline{\xi}_{n\mu} l)}{\left(1 - \frac{\omega_{n\mu}^2}{\omega^2} \right) c_{33}^f G_2^n h^f \overline{\xi}_{n\mu} L_{n\mu}} \quad (\text{A.16})$$

568 in which

$$L_{n\mu} = 2 \left[\int_0^l \overline{f}_{\mu}^n \overline{f}_{\mu}^n dx_1 + \int_l^{\infty} f_{\mu}^{out,n} f_{\mu}^{out,n} dx_1 \right] = l + \frac{\sin(2\overline{\xi}_{n\mu} l)}{2\overline{\xi}_{n\mu}} + \frac{\cos^2(\overline{\xi}_{n\mu} l)}{\overline{\xi}_{n\mu}^{out}} \quad (\text{A.17})$$

569 for $n = m$ and $\mu = \nu$. The current through the square top and bottom
 570 electrodes is

$$\begin{aligned}
 I(\omega, l) &= -(2l)2 \int_0^l j\omega D_3 dx_1 = \\
 &= \frac{4j\omega l^2 \varepsilon_{33}^f V}{h^f} (\widehat{k}^2 + 1) + \frac{8j\omega l V \varepsilon_{33}^f \widehat{k}^2 (G_1^n)^2 (\eta_{fn}^0)^2 \sin^2(\bar{\xi}_{n\mu} l)}{\left(\frac{\widehat{\omega}_{n\mu}^2}{\omega^2} - 1\right) G_2^n (h^f)^2 (\bar{\xi}_{n\mu})^2 L_{n\mu}} \quad (\text{A.18})
 \end{aligned}$$

571 where $D_3 = e_{33}^f \bar{u}_{3,3}^{nf} - \varepsilon_{33}^f \bar{\varphi}_{3,3}^{nf}$, $\widehat{\omega}_{n\mu} = \omega_{n\mu} + j \frac{\omega_{n\mu}}{2Q_{\text{unloaded}}}$, Q_{unloaded} is the un-
 572 loaded quality factor, and $\omega_{n\mu} = 2\pi f_{n\mu}$ the lossless resonance frequency of
 573 the TE_1 -trapped resonator.